J. Fluid Mech. (2007), *vol.* 580, *pp.* 303–318.
doi:10.1017/S0022112007005447 Printed in the United Kingdom

Centrifugal effects in rotating convection: axisymmetric states and three-dimensional instabilities

F. MARQUES,[1] I. MERCADER,[1] O. BATISTE[1] AND J. M. LOPEZ[2]

[1]Departament de Física Aplicada, Univ. Politècnica de Catalunya, Barcelona 08034, Spain
[2]Department of Mathematics and Statistics, Arizona State University, Tempe, AZ 85287, USA

(Received 30 August 2006 and in revised form 11 December 2006)

Rotating convection is analysed numerically in a cylinder of aspect ratio one, for Prandtl number about 7. Traditionally, the problem has been studied within the Boussinesq approximation with density variation only incorporated in the gravitational buoyancy term and not in the centrifugal buoyancy term. In that limit, the governing equations admit a trivial conduction solution. However, the centrifugal buoyancy changes the problem in a fundamental manner, driving a large-scale circulation in which cool denser fluid is centrifuged radially outward and warm less-dense fluid is centrifuged radially inward, and so there is no trivial conduction state. For small Froude numbers, the transition to three-dimensional flow occurs for Rayleigh number $R \approx 7.5 \times 10^3$. For Froude numbers larger than 0.4, the centrifugal buoyancy stabilizes the axisymmetric large-scale circulation flow in the parameter range explored (up to $R = 3.5 \times 10^4$). At intermediate Froude numbers, the transition to three-dimensional flow is via four different Hopf bifurcations, resulting in different coexisting branches of three-dimensional solutions. How the centrifugal and the gravitational buoyancies interact and compete, and the manner in which the flow becomes three-dimensional is different along each branch. The centrifugal buoyancy, even for relatively small Froude numbers, leads to quantitative and qualitative changes in the flow dynamics.

1. Introduction

Rotating Rayleigh–Bénard convection encompasses the competition between rotation and thermal buoyancy in a paradigm problem that incorporates fundamental processes of great importance to atmospheric and oceanic circulations, as well as being of astrophysical importance. Early theoretical work (e.g. Veronis 1959; Chandrasekhar 1961) considered an infinite layer of fluid between two plates maintained at constant temperatures and used the Boussinesq approximation which assumes that density varies linearly with temperature, treats the remaining fluid properties as constants, and density variations are only taken into account in the buoyancy terms.

Traditionally, density variation was only incorporated in the gravitational buoyancy term and not in the centrifugal buoyancy term. This is valid only in the limit of vanishingly small centrifugal force relative to gravity. In this limit, the governing equations admit a trivial conduction solution, where the velocity corresponds to solid body rotation (which is a static state in the rotating frame), together with a linear

temperature profile across the layer. This basic state, being trivial, is independent of all governing parameters. However, when the centrifugal force is not neglected, the basic state is not trivial and depends on many parameters.

The centrifugal buoyancy drives a large-scale circulation in which the cool denser fluid is centrifuged radially outward and the warm less-dense fluid is centrifuged radially inward (Barcilon & Pedlosky 1967; Homsy & Hudson 1969; Hart 2000). This large-scale circulation exists for any non-zero difference in temperature between the top and bottom plate. Neglecting the centrifugal buoyancy allows a straightforward linear stability analysis for the onset of convection from the conduction state; Chandrasekhar (1961) provides a comprehensive account of this for horizontally unbounded fluid layer.

The effects of lateral confinement in rotating convection are of fundamental importance. The experiments of Rossby (1969) found significant discrepancies with the unbounded theory for the onset of rotating convection, measuring convective heat transfer at Rayleigh numbers much lower than predicted. Buell & Catton (1983) and Pfotenhauer, Niemela & Donnelly (1987) proposed, based on linear stability analysis and experiments, that the cause of the discrepancy was the lateral confinement of the experiments. Subsequent experiments, designed to allow flow visualization (Zhong, Ecke & Steinberg 1991, 1993; Ning & Ecke 1993), showed that the convective heat transport recorded at Rayleigh numbers below the predicted critical value was due to a so-called convective wall mode, consisting of alternating hot and cold thermal plumes rising and descending in the cylinder sidewall boundary layer, and precessing retrograde with respect to the rotation of the cylinder. The linear stability analysis of Goldstein *et al.* (1993, 1994) confirmed this picture of the onset of rotating convection due to the combined effects of Coriolis force and lateral confinement in a finite cylinder, in the absence of centrifugal buoyancy. This was further confirmed by the asymptotic analyses of Herrmann & Busse (1993) and Kuo & Cross (1993). The linear stability of the non-trivial basic state incorporating centrifugal buoyancy in a finite cylinder has only been analysed in the asymptotic limit of infinite Coriolis force and steady onset (Homsy & Hudson 1971). A stability analysis for finite values of the parameters and allowing for unsteady non-axisymmetric modes of instability has not been previously presented.

Centrifugal buoyancy destroys the horizontal translation invariance that is inherent in the unbounded theoretical treatments of the problem and the reflection symmetry about the cylinder half-height. When the centrifugal buoyancy is neglected, the onset of convection is via a pitchfork bifurcation when the system is further restricted to an axisymmetric subspace, giving two steady convecting states that are reflections of each other (over a wide range of parameter space, with a sufficiently strong Coriolis force acting, the conduction state is first unstable to the non-axisymmetric wall modes). Centrifugal buoyancy renders the pitchfork bifurcation imperfect, resulting in two distinct branches of (axisymmetric) steady states that are not related by any symmetry (plus an unstable state connecting them). Viewing this problem in terms of varying two parameters, the Froude number and the Rayleigh number, we find that the zero-Froude-number pitchfork bifurcation is a very selective one-parameter path through a codimension-two cusp bifurcation, and that the pair of convective states is part of a non-trivial basic state that lies on a continuous but folded solution manifold. This picture emerges from our computational study in which we computed this basic-state solution manifold using arclength continuation techniques in Rayleigh- and Froude-number parameter space. The linear stability of the axisymmetric solutions to three-dimensional perturbations is analysed, and the results are compared with

previous studies, shedding new light on the relevance of the centrifugal buoyancy in rotating Rayleigh–Bénard convection.

2. Governing equations and numerical scheme

Consider the flow in a circular cylinder of radius r_0 and depth d, rotating at a constant rate $\omega\,\mathrm{rad\,s^{-1}}$. The top endwall is maintained at a constant temperature $T^* = T_0 - 0.5\Delta T$ and the bottom endwall at a constant temperature $T^* = T_0 + 0.5\Delta T$. In the rotating frame of reference, the Navier–Stokes equations are

$$\rho(\partial_t + \boldsymbol{u}\cdot\nabla)\boldsymbol{u} = -\nabla p^* + \nabla\cdot(\mu\nabla\boldsymbol{u}) - \rho g\hat{\boldsymbol{z}} + 2\rho\omega\boldsymbol{u}\times\hat{\boldsymbol{z}} + \rho\omega^2\boldsymbol{r}, \tag{2.1}$$

where $\boldsymbol{u}$ is the velocity field in the rotating frame, p^* is the pressure, μ is the shear viscosity, g is the gravitational acceleration, $\hat{\boldsymbol{z}}$ the unit vector in the vertical direction z, and $\boldsymbol{r}$ is the radial vector in cylindrical coordinates. To lowest order, the density varies linearly with temperature, i.e. $\rho = \rho_0[1 - \alpha(T^* - T_0)] = \rho_0(1 - \alpha T)$, where α is the coefficient of volume expansion, T_0 is the mean temperature, $T = T^* - T_0$ is the temperature deviation (which we refer to simply as the temperature from now on) and ρ_0 is the density at T_0. The Boussinesq approximation treats all fluid properties as constant, except for the density. Any term in equation (2.1) with a factor ρ can be split into two terms, one with a factor ρ_0 and the other with a factor $-\rho_0\alpha T$. If the ρ_0 term is not a gradient, it is the leading-order term, and the associated $-\rho_0\alpha T$ term may be neglected. If it is a gradient, it can be absorbed into the pressure gradient, and the associated $-\rho_0\alpha T$ term must be retained. The only ρ_0 terms that are gradients are

$$-\rho_0 g\hat{\boldsymbol{z}} + \rho_0\omega^2\boldsymbol{r} = \nabla(-\rho_0 g z + \rho_0\omega^2 r^2/2), \tag{2.2}$$

and so the only terms with density variations that remain are the gravitational and the centrifugal buoyancies. The Navier–Stokes–Boussinesq equations for rotating convection are (2.1) plus the temperature equation and the incompressibility condition:

$$(\partial_t + \boldsymbol{u}\cdot\nabla)\boldsymbol{u} = -\nabla p + \nu\nabla^2\boldsymbol{u} + g\alpha T\hat{\boldsymbol{z}} + 2\omega\boldsymbol{u}\times\hat{\boldsymbol{z}} - \omega^2\alpha T\boldsymbol{r}, \tag{2.3}$$

$$(\partial_t + \boldsymbol{u}\cdot\nabla)T = \kappa\nabla^2 T, \qquad \nabla\cdot\boldsymbol{u} = 0, \tag{2.4}$$

where $p = p^*/\rho_0 + gz - \omega^2 r^2/2$ is the kinematic pressure including gravitational and centrifugal contributions, ν is the kinematic viscosity, and κ is the thermal diffusivity.

The system is non-dimensionalized using d as the length scale, d^2/κ as the time scale, and ΔT as the temperature scale. There are five non-dimensional parameters: the Rayleigh number $R = \alpha g d^3\Delta T/\kappa\nu$, the Coriolis number $\Omega = \omega d^2/\nu$, the Froude number $F = \omega^2 r_0/g$, the Prandtl number $\sigma = \nu/\kappa$, and the aspect ratio $\gamma = r_0/d$. The non-dimensional cylindrical domain is $(r, \theta, z) \in [0, \gamma] \times [0, 2\pi) \times [-1/2, 1/2]$. The resulting equations (from now on, $\boldsymbol{u}$, T and p are dimensionless quantities) are

$$(\partial_t + \boldsymbol{u}\cdot\nabla)\boldsymbol{u} = -\nabla p + \sigma\nabla^2\boldsymbol{u} + \sigma RT\hat{\boldsymbol{z}} + 2\sigma\Omega\boldsymbol{u}\times\hat{\boldsymbol{z}} - \frac{\sigma F R}{\gamma}T\boldsymbol{r}, \tag{2.5}$$

$$(\partial_t + \boldsymbol{u}\cdot\nabla)T = \nabla^2 T, \qquad \nabla\cdot\boldsymbol{u} = 0. \tag{2.6}$$

The boundary conditions for $\boldsymbol{u}$ and T are

$$r = \gamma: \qquad T_r = u = v = w = 0, \tag{2.7}$$

$$z = \pm 1/2: \quad T = \mp 0.5, \; u = v = w = 0, \tag{2.8}$$

where (u, v, w) are the components of $\boldsymbol{u}$ in cylindrical coordinates.

The governing equations are invariant under rotations around the axis of the cylinder. If the Froude number is zero, the governing equations are also invariant to a reflection K_z about the half-height $z=0$, whose action is $K_z(u, v, w, T, p)(r, \theta, z) = (u, v, -w, -T, p)(r, \theta, -z)$. For axisymmetric solutions it is convenient to introduce a streamfunction ψ, where $u=-\psi_z/r$ and $w=\psi_r/r$. The action of the reflection K_z on the streamfunction is $K_z\psi(r, \theta, z) = -\psi(r, \theta, -z)$.

2.1. *Numerical method*

The governing equations have been solved using the second-order time-splitting method proposed in Hughes & Randriamampianina (1998) combined with a pseudo-spectral method for the spatial discretization, utilizing a Galerkin–Fourier expansion in the azimuthal coordinate θ and Chebyshev collocation in r and z. The radial dependence of the variables is approximated by a Chebyshev expansion between $-\gamma$ and γ and enforcing their proper parities at the origin (Fornberg 1998). Specifically, the scalar field T has even parity $T(-r, \theta, z) = T(r, \theta + \pi, z)$, as does the vertical velocity w, whereas u and v have odd parity. To avoid including the origin in the collocation mesh, an odd number of Gauss–Lobatto points in r is used and the equations are solved only in the interval $(0, \gamma]$. Following Orszag & Patera (1983), we have used the combinations $u_+ = u + \mathrm{i}v$ and $u_- = u - \mathrm{i}v$ in order to decouple the linear diffusion terms in the momentum equations. For each Fourier mode, the resulting Helmholtz equations for T, w, u_+ and u_- have been solved using a diagonalization technique in the two coordinates r and z. The imposed parity of the functions guarantees the regularity conditions at the origin needed to solve the Helmholtz equations (Mercader, Net & Falqués 1991).

Steady solutions have been computed by Newton's method. We have used a first-order version of the time-stepping code described above for the calculation of a Stokes preconditioner that allows a matrix-free invertion of the preconditioned Jacobian needed in each Newton iteration (Mamun & Tuckerman 1995). The corresponding linear system is solved by an iterative technique using a GMRES package (Frayssé, Giraud & Langou 2003); with this method the Jacobian matrix is never constructed nor stored. In order to follow steady solution branches we use an arclength continuation algorithm that allows either the Rayleigh number or the Froude number to vary during the continuation process (Bergeon *et al.* 1998). The same techniques have proven to be efficient calculating and following rotating wave solutions (Mercader, Batiste & Alonso 2006).

We have used 36 spectral modes in z and r and a time step $\mathrm{d}t = 2 \times 10^{-5}$ thermal time units in all computations; for the linear stability analysis and three-dimensional computations, azimuthal wavenumbers up to 10 have been considered.

3. Axisymmetric solution manifold

The problem depends on five non-dimensional parameters, and a comprehensive parametric analysis would be prohibitive. We have fixed $\gamma = 1$ to avoid very large azimuthal wavenumber modes, and $\sigma = 7.0$ which essentially corresponds to water near room temperature. We wish to analyse the relative importance of the gravitational buoyancy (characterized by R) and the centrifugal buoyancy (characterized by F) in a rotating system (the Coriolis acceleration being characterized by Ω). In a physical experiment, Ω and F vary simultaneously with the rotation frequency ω and either both are zero or both are different from zero. However, the classical treatment of

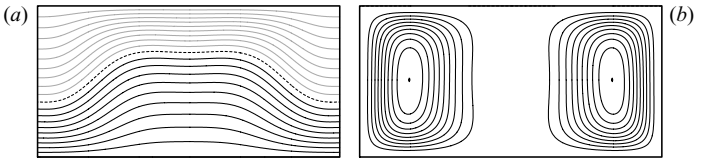

FIGURE 1. (*a*) Isotherms and (*b*) streamlines of the base state at $R = 1.1 \times 10^4$ and $F = 0.4$, in a meridional plane where the left and right vertical boundaries shown are the cylinder sidewall at $r = \gamma$ and $\theta = 0$ and π. There are 10 positive (black) and 10 negative (grey) linearly spaced contour levels in the ranges $T \in [-0.5, 0.5]$ and $\psi \in [0, 0.8]$.

the problem has been to take $F = 0$ and $\Omega \neq 0$, corresponding to the singular limit $g \to \infty$. Here, we fix $\Omega = 100$, and consider variations in R and F.

3.1. *The centrifugally dominated solution*

In the absence of centrifugal buoyancy ($F = 0$), the basic state is the conductive state where the fluid is in solid-body rotation with a linear temperature profile: $T = -z$ and $\boldsymbol{u} = 0$. For non-zero Froude number, the basic state is more complex: the cool fluid near the top of the cylinder is centrifuged radially outward while the warm fluid close to the bottom is centrifuged radially inward. Figure 1 shows isotherms T and streamlines ψ, plotted in a meridional plane, for $R = 1.1 \times 10^4$ and Froude number $F = 0.4$. For the aspect ratio considered, $\gamma = 1$, a single axisymmetric recirculation cell results, with a wide almost uniform upwelling of warm fluid near the centre, whose strength increases with increasing Froude number.

For $R < R_{C_1} = 1.115 \times 10^4$, a single stable state exists for a given point (F, R) in parameter space. At $(F, R) = (0, R_{C_1})$ there is a codimension-two cusp bifurcation which gives rise to regions of parameter space with multiple solutions.

3.2. *The primary cusp bifurcation C_1*

The base state as a function of F has been computed using continuation for several values of R. Figure 2(*a*) shows sections of the base-state solution manifold, using the temperature T_c on the axis at half-height ($r = z = 0$) as a measure of the flow state. The solution curves have been formally extended to negative values of F. The continuation process uses arclength continuation, and F is a function of the arclength. During the continuation process, F changes sign several times, depending on R. If we restrict to $F \geqslant 0$, the continuation curve obtained would consist of disjoint segments that in fact are part of the same smooth continuation curve if negative F values are allowed. Although negative values of F cannot be physically realized ($F = \omega^2 r_0 / g \geqslant 0$), they reflect the action of the K_z symmetry on the system, which is invariant to K_z only when $F = 0$. The resulting extended solution curve is symmetric about the origin $(F, T_c) = (0, 0)$. When $F \neq 0$ the system is not K_z invariant: the action of K_z changes the sign of the centrifugal buoyancy term in (2.5). However, the action of K_z on a solution with $F > 0$ results in a solution of (2.5) with Froude number value $-F$. A negative value of F can be interpreted as a centripetal acceleration, advecting denser fluid in toward the axis and lighter fluid radially outward.

At $R = 1.1 \times 10^4$ the section of the solution manifold is single-valued, but for $R > R_{C_1} = 1.115 \times 10^4$, the section is multi-valued for F near zero. At R_{C_1} the solution manifold develops a twist as shown schematically in figure 2(*b*). The curve section $R = R_{C_1}$ has a vertical tangent at $F = 0$. This corresponds to a cusp bifurcation. Cross-sections of the solution manifold at constant R values correspond to the curves

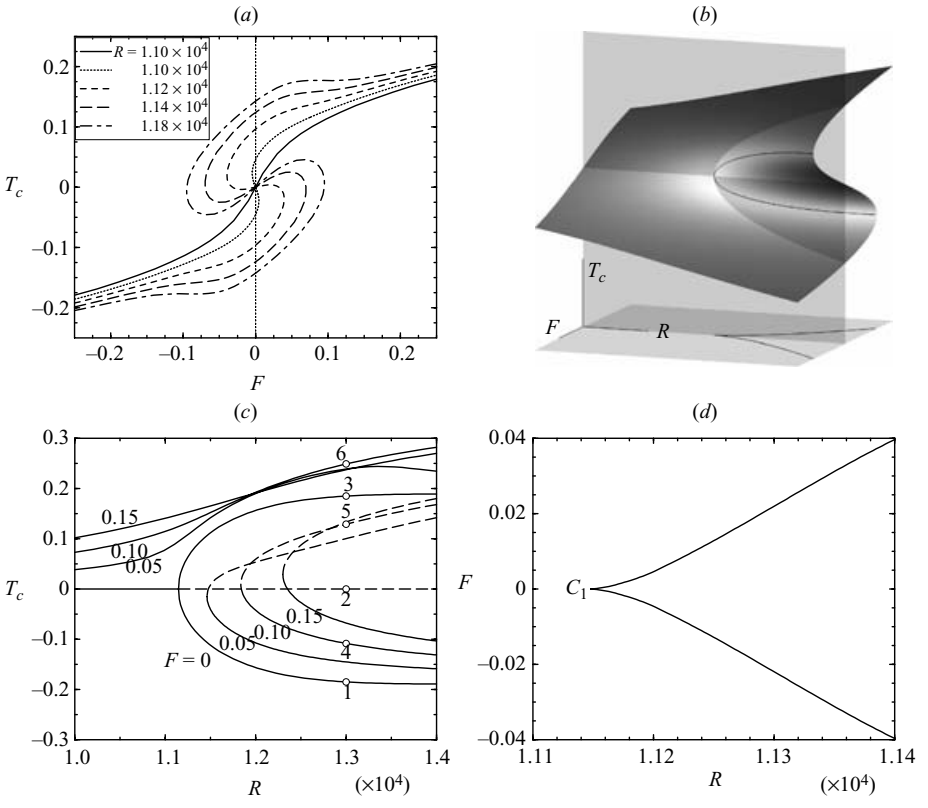

FIGURE 2. (*a*) Sections of the base-state solution manifold for various R as indicated. (*b*) Schematic of the base-state solution manifold. (*c*) Sections of the base-state solution manifold for various F as indicated. Isotherms of the states at points marked with ○ and labelled 1 to 6 are shown in figure 3. Stable (unstable) solutions are shown as solid (dashed) lines. (*d*) Projection of the saddle-node bifurcation curves, emerging from the cusp point C_1, onto the (R, F) plane.

in figure 2(*a*). Cross-sections at constant F values are shown in figure 2(*c*). The cross-section at $F = 0$ is a pitchfork bifurcation, where the conductive state (with $T_c = 0$) loses stability at R_{C_1} and two stable (in the axisymmetric subspace) solutions are born, symmetrically related by K_z. The Froude number acts as an unfolding parameter, breaking the K_z symmetry; the pitchfork bifurcation becomes part of the codimension-two cusp bifurcation. For small values of F we have an imperfect pitchfork: one of the branches is the centrifugal branch and extends smoothly to $R = 0$, while the other two branches are disconnected, appearing at a saddle-node bifurcation at a critical value of R, as illustrated in figure 2(*c*). In the extended view of the system including $F < 0$, there are two loci of saddle-node bifurcations which meet at the cusp bifurcation point C_1, at $F = 0$ and $R = R_{C_1}$; their projections onto the (R, F) plane are shown in figure 2(*d*).

Figure 3 shows isotherms at $R = 1.3 \times 10^4$ of the three solutions at (*a*) $F = 0$ and (*b*) $F = 0.1$. For $F = 0$ the solutions labelled 1 and 3 are K_z-reflections of each other and the solution labelled 2 is the trivial conduction state. The centrifugal buoyancy drives the cold fluid down the sidewall for all three $F = 0.1$ solutions labelled 4, 5 and 6. Since the centrifugal force varies linearly with the radial distance, its effects near

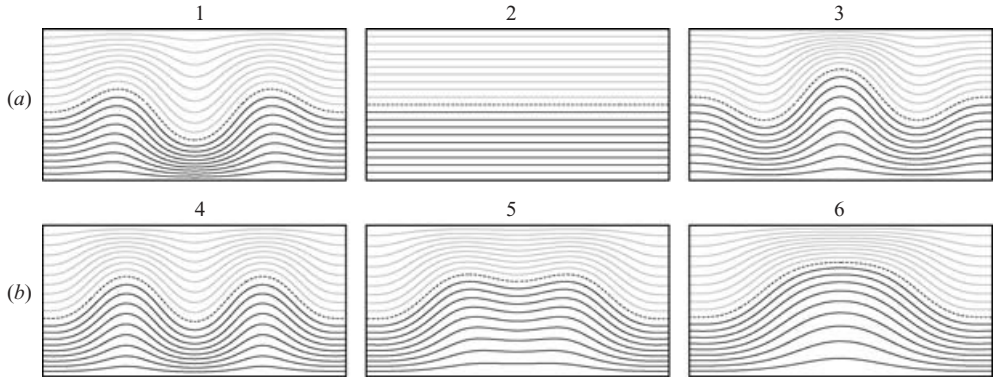

FIGURE 3. Isotherms at $R = 1.3 \times 10^4$: (*a*) three coexisting states at $F = 0$ on the pitchfork, as shown in figure 2(*c*), labelled 1, 2 and 3; (*b*) three coexisting states at $F = 0.1$ on the imperfect pitchfork, as shown in figure 2(*c*), labelled 4, 5 and 6.

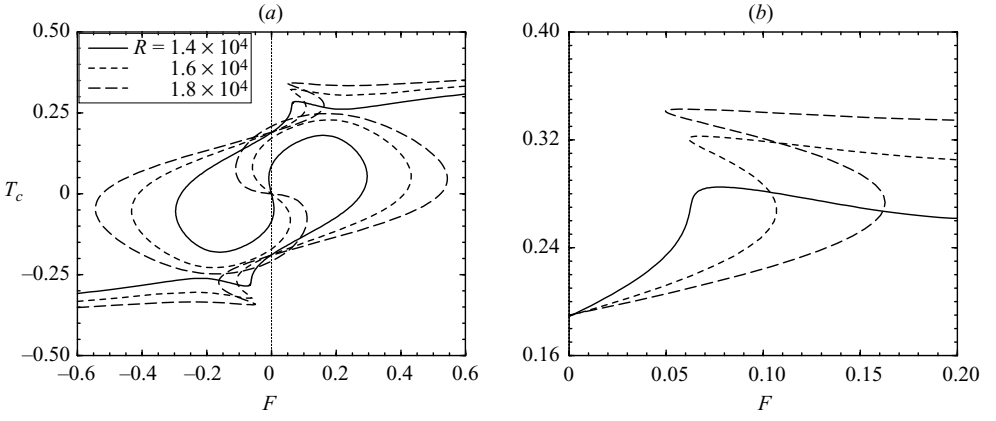

FIGURE 4. (*a*) Sections of the base-state solution manifold for various R as indicated, and (*b*) an enlargement showing the formation of the secondary cusp C_3.

the axis are negligible. On the solution labelled 6 the centrifugal buoyancy reinforces the strong upwelling at the axis, whereas on 4 the upwelling occurs via a toroidal ring at $r \approx 0.5$ and is accompanied by a cold thermal plume descending on the axis. The unstable solution 5 is roughly the average of solutions 4 and 6. Considering these various solutions at fixed R, one may think of them as belonging to distinct solution branches. However, they are all continuous on a single solution manifold as illustrated schematically in figure 2(*b*).

3.3. *Secondary cusp bifurcations C_2 and C_3*

As R is increased beyond 1.3×10^4, the base solution manifold becomes more twisted as further cusp bifurcations occur. Figure 4(*a*) shows three sections of the manifold at $R = 1.4 \times 10^4$, 1.6×10^4 and 1.8×10^4. At $R = 1.4 \times 10^4$, the slope of the section at $(F, T_c) = (0, 0)$ is negative, indicating that the conduction state (which had already lost stability at $R = R_{C_1} \approx 1.115 \times 10^4$) has undergone a secondary cusp bifurcation C_2 at $R = R_{C_2} \approx 1.342 \times 10^4$, and the associated saddle-node bifurcations are identified in the figure as the points near $(F, T_c) = (0, 0)$ where the slope of the section is vertical. Linear stability analysis reveals that the conduction state following the secondary

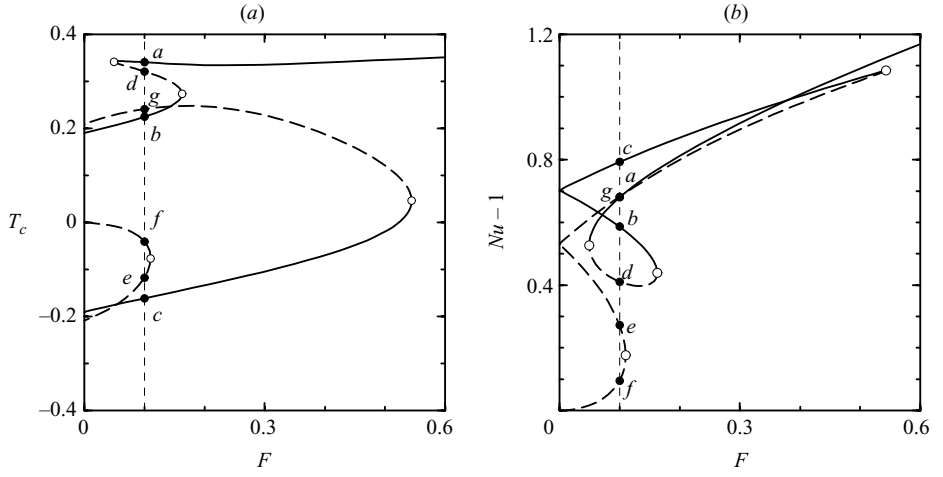

FIGURE 5. Section of the base solution manifold at $R = 1.8 \times 10^4$, characterized by (*a*) T_c and (*b*) the Nusselt number. The solid (dashed) lines correspond to stable (unstable) states in the axisymmetric subspace. The vertical dashed line at $F = 0.1$ intersects the solution manifold at seven distinct points (labelled *a*–*g*, corresponding isotherms are shown in figure 6) at one point in parameter space, $(F, R) = (0.1, 1.8 \times 10^4)$.

cusp bifurcation C_2 remains unstable, as are the solutions on the portion of the section between the two saddle-nodes emerging from the cusp.

Figure 4(*b*) is an enlargement of the region near $(F, T_c) = (0.1, 0.25)$, which shows the development of a cusp bifurcation of the centrifugally dominated convective state as R is increased from 1.4×10^4 to 1.6×10^4. The section in this region becomes vertical at the cusp point C_3 at $(F, R) = (0.0646, 1.418 \times 10^4)$. Before the cusp bifurcation, the convective solution was stable, and following the bifurcation the section in the fold between the two emergent saddle-node bifurcations is unstable and the rest is stable.

Figure 5(*a*) shows in more detail the stability of the solutions in the different segments of the section at $R = 1.8 \times 10^4$; the solid curves are stable, and the dashed curves are unstable in the axisymmetric subspace. There are up to seven distinct coexisting solution states for a given value of F. The dashed line at $F = 0.1$ intersects the solution manifold at seven distinct points. Figure 5(*b*) shows the same solution manifold in terms of the Nusselt number, Nu, rather than T_c. The solutions that are stable tend to have the largest Nu. Furthermore, for $F > 0.544$ the centrifugally dominated solution is the only solution and its Nusselt number increases monotonically with F.

Figure 6 shows isotherms of the seven coexisting solutions at the single point in parameter space $(F, R) = (0.1, 1.8 \times 10^4)$ labelled in figure 5. The three solutions (*a*), (*b*) and (*c*) are stable in the axisymmetric subspace. Solution (*a*) is centrifugally dominated, belonging to the upper segment in figure 5(*a*), beginning at a saddle-node bifurcation and extending to $F \to \infty$. The corresponding segments for different R constitute the centrifugal branch CB. The other two stable solutions are characterized by upwelling plumes on the axis and the sidewall for solution (*b*) and downwelling plumes on the axis and the sidewall for solution (*c*). Solutions (*b*) and (*c*) constitute the downwelling (DB) and upwelling (UB) branches. The other solutions shown in figure 6 are unstable.

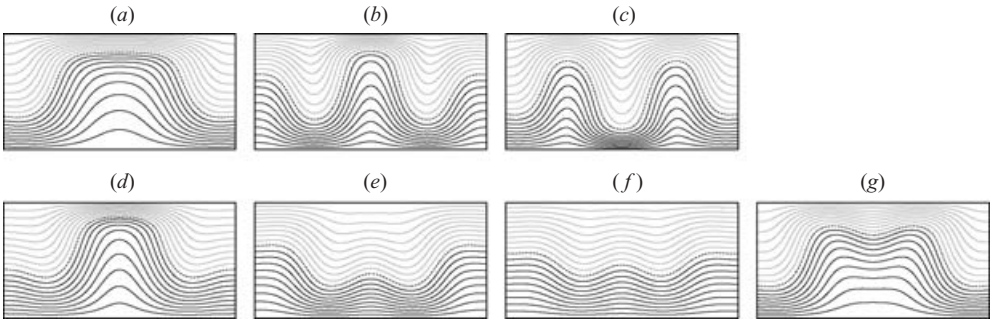

FIGURE 6. Isotherms of solutions on the base-state manifold at $R = 1.8 \times 10^4$ corresponding to the seven different solutions coexisting at the one point in parameter space $(F, R) = (0.1, 1.8 \times 10^4)$, labelled in figure 5. The states (a)–(c) are stable in the axisymmetric subspace and (d)–(g) are unstable.

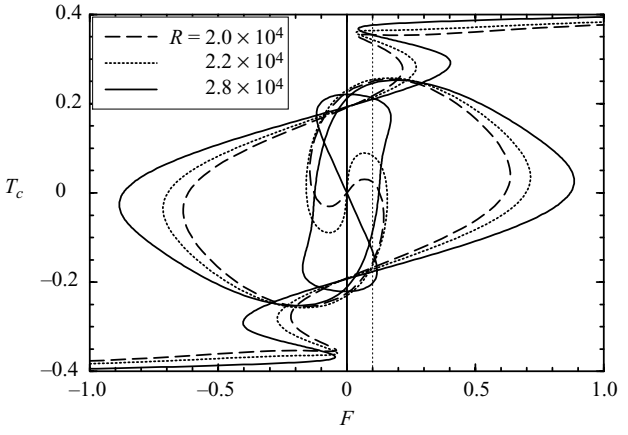

FIGURE 7. Sections of the base-state solution manifold for various R as indicated.

The solution manifold becomes more twisted generating more coexisting solutions as R is increased. At $(F, R) = (0, 22422)$, a further cusp bifurcation, C_4, of the trivial conduction state takes place, as illustrated by the sections of the solution manifold in figure 7. For example, by $R = 2.8 \times 10^4$ for $F = 0.1$, there are nine coexisting states (the vertical dashed line at $F = 0.1$ in the figure intersects the manifold nine times). We have continued the solution manifold out to $R = 3.5 \times 10^4$ and no further bifurcations were found. Figure 8(a) is a bifurcation diagram showing the codimension-two cusp bifurcations C_1, C_2, C_3 and C_4, and the saddle-node bifurcation curves emerging from them. Note that the saddle-node bifurcation curves do not interest each other, they just appear to do this in the projection onto the (R, F) parameter space. Also indicated in the figure are the numbers of coexisting axisymmetric solutions in different regions of parameter space. The extensions of the cusps and saddle-node bifurcations to $F < 0$ are included as dotted curves. Figure 8(b) shows the sections of the cusp bifurcations at $F = 0$: they are pitchfork bifurcations due to the K_z symmetry. The different solutions emerging from the pitchfork bifurcations are labelled with the number of positive eigenvalues determined from their linear stability analysis in the axisymmetric subspace.

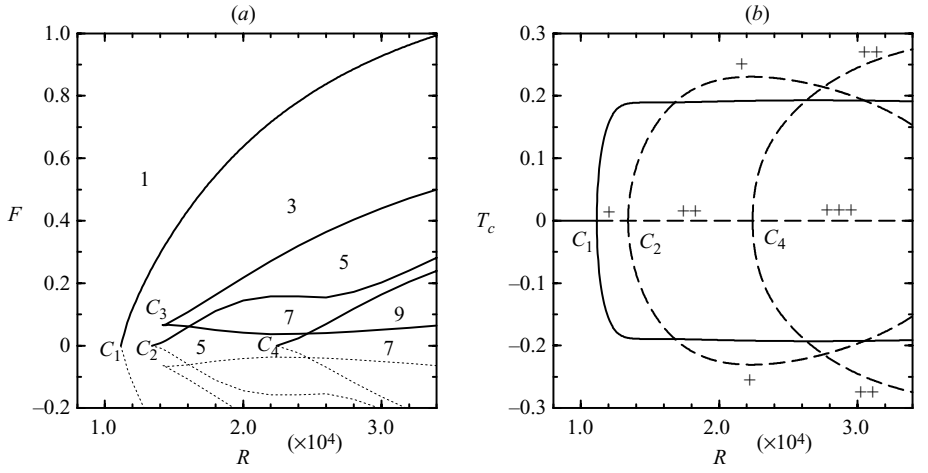

FIGURE 8. (*a*) Bifurcation diagram showing the codimension-two cusp bifurcations C_1, C_2, C_3 and C_4, and the saddle-node bifurcation curves emerging from them. (*b*) The pitchfork bifurcations corresponding to the cusp bifurcations C_1, C_2 and C_4 in the one-parameter path with $F = 0$. Solid (dashed) curves correspond to stable (unstable) states in the axisymmetric subspace; the '+' symbols indicate how many eigenvalues with positive real part are associated with the unstable states.

4. Linear stability of axisymmetric solutions to three-dimensional perturbations

There are three different branches of solutions that are stable in the axisymmetric subspace: the centrifugal *CB*, upwelling *UB*, and downwelling *DB* branches (shown at $R = 1.8 \times 10^4$ in figure 5 as the three solid curves). Figures 6(*a*), 6(*b*) and 6(*c*) show isotherms of the three branches *CB*, *UB* and *DB*, respectively. Solutions that are unstable in the axisymmetric subspace continue to be unstable in the full space. Nevertheless, it is important to characterize these unstable solutions as they may be involved in global bifurcations, such as saddle-loop homoclinics and saddle-node-invariant-circle bifurcations; the latter, for example, lead to radially travelling waves in convection in a cylinder (Barkley & Tuckerman 1988; Lopez, Rubio & Marques 2006).

It is well known that, for $F = 0$, the primary instability of the trivial conduction state is three-dimensional, and wall modes consisting of alternating upward and downward thermal plumes close to the sidewall are the dominant instability mechanism at the Prandtl number σ, Coriolis number Ω, and aspect ratio γ considered here (Goldstein *et al.* 1993). Here, we investigate the stability of the non-trivial axisymmetric states. Simultaneously with the arclength continuation, we compute the most dangerous eigenvalues of the axisymmetric solutions using Krylov methods, determining the growth rate and frequency of the different azimuthal wavenumber perturbations.

The upwelling branch *UB* is unstable to three-dimensional perturbations for all parameter values considered here. Typical isotherms for this state are shown in figure 6(*b*). The upwelling of warm fluid at the sidewall flows against the large-scale circulation (LSC) driven by the centrifugal force, and so it is not surprising that this state is unstable.

4.1. *Stability analysis of the downwelling state*

Typical isotherms for the downwelling state *DB* are shown in figure 6(*c*). They are very similar to those of the centrifugal state *CB* (figure 6*a*), except for the downwelling

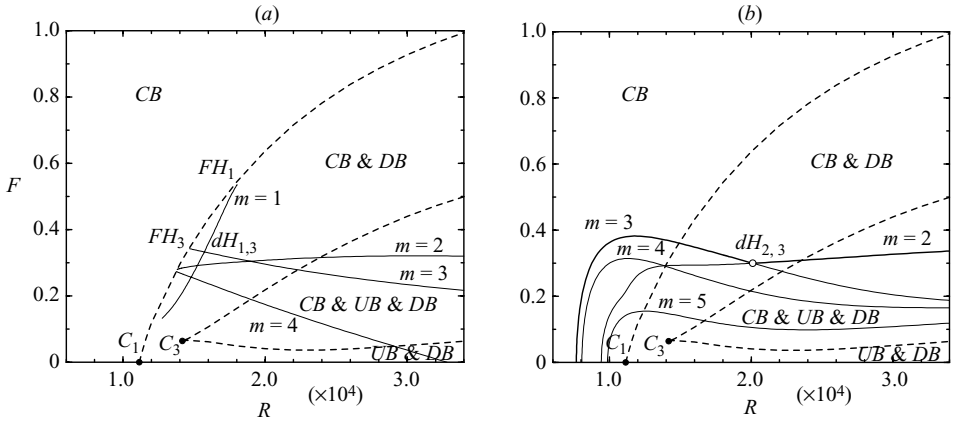

FIGURE 9. Three-dimensional instabilities of the (*a*) downwelling and (*b*) centrifugal branches. *DB* is stable to three-dimensional perturbations in the narrow triangular region delimited by the saddle-node curve emerging from C_1 and the Hopf curves to $m = 1$ and $m = 3$ rotating waves; *CB* is stable for all R considered, for sufficiently large $F > 0.4$.

cold plume on the cylinder axis. The stability properties of the downwelling branch are summarized in figure 9(*a*). The dashed lines in this figure are saddle-node curves at which *CB*, *UB* and *DB* branches are born. These curves are the solid lines in figure 8(*a*) emanating from the cusp bifurcation points C_1 and C_3, and they delineate the regions of (R, F)-parameter space in which these axisymmetric solutions exist. The solid lines are Hopf bifurcation curves where the *DB* solution becomes unstable to three-dimensional perturbations with azimuthal wavenumber m as indicated on the figure. The *DB* solution only exists to the right of the left-most saddle-node curve emerging from the cusp point C_1, and it is stable only in the small triangular region delimited by the saddle-node curve to the left, the Hopf bifurcation to the $m = 1$ curve to the right, and the Hopf bifurcation to the $m = 3$ curve at the bottom. All the other Hopf bifurcations of *DB* are secondary as *DB* is already unstable to $m = 1$ or 3. The vertices of this triangular region are codimension-two bifurcation points: two fold-Hopf bifurcations FH_1 and FH_3, and the double-Hopf bifurcation $dH_{1,3}$. There is often complex dynamics associated with these codimension-two bifurcations (Kuznetsov 1998), suggesting the possibility of complex nonlinear dynamics in the neighbourhood of this region.

Figure 10(*a*) shows isotherms of the $m = 3$ eigenmode of the *DB* axisymmetric state at $R = 1.5 \times 10^4$ and $F = 0.3$ at various depths. It is a wall mode born at a supercritical Hopf bifurcation with frequency of about 9.04. The resulting limit cycle is a rotating wave with three rising hot and three descending cold plumes near the sidewall and precessing retrograde with respect to the system rotation with precession period $\tau = 2\pi/9.04 \approx 0.695$. Figure 10(*b*) shows isotherms of the $m = 1$ eigenmode of the *DB* axisymmetric state at $R = 1.8 \times 10^4$ and $F = 0.4$ at various depths. It is a body-mode perturbation that comes about at a supercritical Hopf bifurcation with Hopf frequency of about 0.227. The resulting limit cycle is an $m = 1$ precession of the cold thermal plume descending on the axis. The precession is prograde with respect to the system rotation with precession period $\tau = 2\pi/0.227 \approx 27.6$. Note that the $m = 3$ wall mode is a fast mode ($\tau \approx 0.7$) and that the $m = 1$ body mode is a slow mode ($\tau \approx 28$). The wall and body modes of the conduction state are likewise fast and slow, and also precess retrograde and prograde respectively (Goldstein *et al.* 1993). The

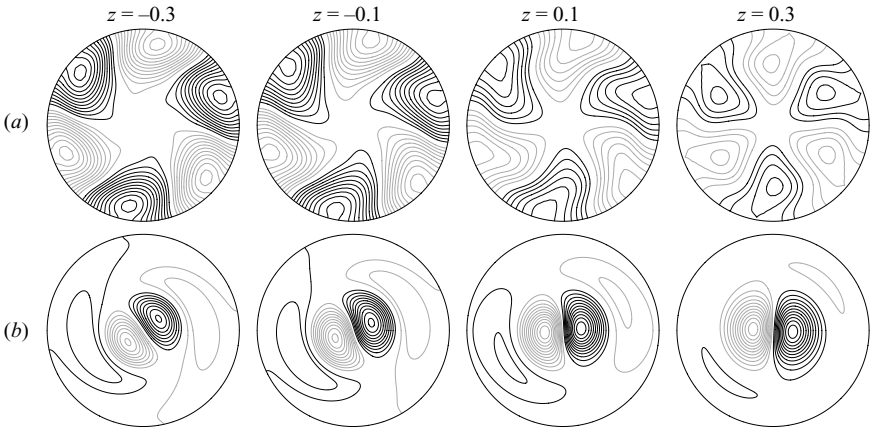

FIGURE 10. Isotherms of the critical eigenmodes of the *DB* axisymmetric state, in horizontal planes at z-levels as indicated. (*a*) $m=3$, $R=1.5\times10^4$, $F=0.3$, and (*b*) $m=1$, $R=1.8\times10^4$, $F=0.4$. There are 12 positive (black) and 12 negative (grey) uniformly spaced contours between the minimum and maximum of the temperature eigenfunction.

remaining critical modes $m=2$ and $m=4$ in figure 9(*a*), which are never dominant critical modes, are wall modes.

4.2. *Stability analysis of the centrifugal state*

Typical isotherms for the centrifugal state are shown in figure 6(*a*). The stability properties of the centrifugal branch *CB* are summarized in figure 9(*b*). The *CB* branch exists for all values of the parameters (R, F) except below the lower dashed line emanating from C_3; this line is the saddle-node curve where the *CB* solution disappears. The solid lines are Hopf bifurcation curves where the *CB* solution becomes unstable to three-dimensional perturbations with azimuthal wavenumber m as indicated in the figure. The primary instabilities of *CB* are supercritical Hopf bifurcations to precessing wall modes with $m=3$ for $R<2.02\times10^4$ and $m=2$ for $R>2.02\times10^4$; *CB* is stable to three-dimensional perturbations above these two Hopf curves, which intersect at the double Hopf bifurcation point $(R, F)=(2.01\times10^4, 0.30002)$. The Hopf bifurcation to an $m=3$ wall mode at $F=0$ is the primary instability of the conduction state studied in Goldstein *et al.* (1993). Their linear stability analysis of the conduction state at $\gamma=1$, $\Omega=100$ and $\sigma=6.7$ (we have studied $\sigma=7.0$) shows that a supercritical Hopf bifurcation to an $m=3$ retrograde precessing wall mode occurs at $R\approx7.5\times10^3$ with a Hopf frequency of about 15, corresponding to a precession period of about 0.42. This agrees very well with the estimates using the present numerical techniques, which give onset at $R=7.67\times10^3$ with Hopf frequency of 15.29. Figure 11(*a*) shows isotherms of the $m=3$ eigenmode of the conduction state at $R=8\times10^3$ and $F=0$ at various depths. The resulting limit cycle is a rotating wave with three hot rising and three cold descending plumes near the sidewall and precessing retrograde with respect to the system rotation with precession period $\tau\approx0.393$. This eigenmode is K_z symmetric, with the maximum of the perturbation at half-height $z=0$. Its structure is very similar to the $m=3$ eigenmode of *DB* discussed above, the main difference being that the eigenmode of *DB* is not K_z symmetric owing to the centrifugal buoyancy driving an LSC.

For $F\neq0$, the Hopf bifurcation to $m=3$ of the conduction state becomes the Hopf bifurcation to $m=3$ of the centrifugal state *CB*. Figure 11(*b*) shows isotherms

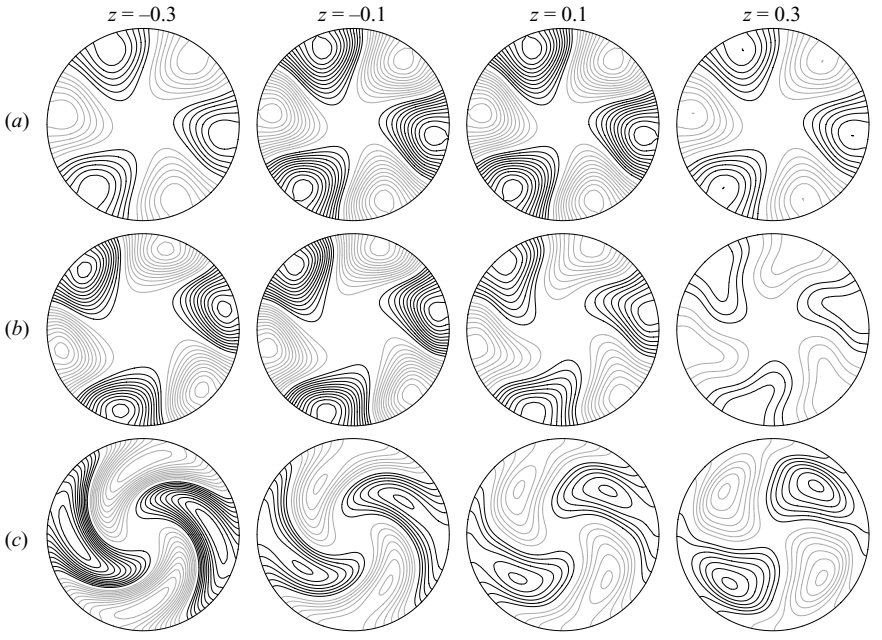

FIGURE 11. Isotherms of the eigenmodes of the *CB* in horizontal planes at z-levels as indicated. (*a*) $m=3$, $R=8\times10^3$, $F=0$ (conductive state), (*b*) $m=3$, $R=1.2\times10^4$, $F=0.35$, (*c*) $m=2$, $R=3\times10^4$, $F=0.3$. There are 12 positive (black) and 12 negative (grey) uniformly spaced contours between the minimum and maximum of the temperature eigenfunction.

of the corresponding eigenmode at $R=1.2\times10^4$ and $F=0.35$ at various depths. The centrifugal buoyancy has broken the K_z symmetry; the temperature eigenfunction has its maximum near the bottom plate, as is the case with the $m=3$ eigenmode of *DB*. The resulting wall mode precesses retrograde with a period $\tau\approx0.496$ at this point in parameter space.

Figure 11(*c*) shows isotherms of the $m=2$ eigenmode of the centrifugal state *CB* at $R=3\times10^4$ and $F=0.3$ at various depths. The temperature eigenfunction has its maximum near the bottom plate. It is another wall mode, a rotating wave with two hot rising and two cold descending plumes near the sidewall and precessing prograde with respect to the system rotation with precession period $\tau\approx0.372$.

5. Discussion and conclusions

Centrifugal buoyancy drives a large-scale circulation, LSC, which has a dramatic impact on the basic states over an extensive range of parameter space. The axisymmetric LSC suffers a number of axisymmetric cusp bifurcations as R is increased. When viewed in a parameter space formally extended to negative Froude numbers, these cusp bifurcations are seen to be associated with the twisting of the LSC solution manifold. This twisted structure of the LSC solution manifold was determined by using an arclength continuation technique. In the range of parameters considered, we have found up to nine coexisting axisymmetric solution states at a single point in parameter space. Of all these solutions, only three are ever stable in the axisymmetric subspace. One of these, the centrifugal branch, exists in almost all parameter space explored, and is basically the centrifugally driven LSC. Linear

stability analysis of these three solution branches reveals that they become unstable to three-dimensional perturbations via Hopf bifurcations in certain regions of parameter space. In the limit of zero centrifugal force ($F \to 0$), the associated conduction state is unstable to a succession of bifurcations (both axisymmetric and non-axisymmetric) over a very short range of R. For sufficiently strong Coriolis force, the primary instability of the conduction state is a Hopf bifurcation to a wall mode. For small centrifugal force (when $\gamma = 1$, $\sigma = 7$ and $\Omega = 100$, the small centrifugal force range corresponds to $F < 0.05$), F acts as a small imperfection parameter, softening the bifurcations in the $F = 0$ idealization and producing similar dynamics. In fact, for $R > R_{C_3}$ and $F < 0.05$, the centrifugal branch ceases to exist, and the two existing axisymmetric states UB and DB come about from the pitchfork bifurcation at $F = 0$. Experimental results specifically designed to minimize the centrifugal buoyancy have typically agreed well with theoretical and numerical results with $F = 0$ that have incorporated physically realistic boundary conditions (Bodenschatz, Pesch & Ahlers 2000; Sánchez-Álvarez *et al.* 2005).

For $F > 0.4$, the flow properties change radically: the axisymmetric centrifugal branch remains linearly stable to three-dimensional perturbations with m at least up to 10 and for R at least up to 3.5×10^4 (the largest m and R we have investigated so far); this centrifugally driven axisymmetric LSC is very robust and completely dominates the convection problem with fast rotation. The UB branch ceases to exist for $F > 0.5$ and is never stable to three-dimensional perturbations; it is very likely that this is because the fluid at the sidewall flows against the LSC driven by the centrifugal force. The fluid flow of the DB branch is very similar to the flow in the centrifugal branch, except for the presence of a downwelling cold plume on the cylinder axis. The stability properties of DB for $m > 1$ (wall modes) are very similar to the stability properties of CB, as can be seen from comparing figures 9(a) and 9(b). However, the $m = 1$ perturbation destabilizes the flow, and the DB state is only stable in a small triangular region in parameter space (see figure 9a). This instability mode corresponds to a precession of the downwelling cold plume on the cylinder axis.

For moderate Froude numbers, $F \in (0.05, 0.4)$, the axisymmetric basic states also become unstable to modes similar to those that the $F = 0$ conduction state becomes unstable to, but the critical Rayleigh numbers at which instability sets in are increasingly larger with increasing F. In fact, the CB branch becomes stable to three-dimensional perturbations with a given m for F sufficiently large in $F \in (0.05, 0.4)$. In this region a sequence of codimension-two bifurcations takes place, that includes cusp, fold-Hopf and double Hopf bifurcations. These occur in close proximity of each other in (R, F) parameter space, and one can expect to find complex nonlinear dynamics nearby.

There are very few systematic experimental studies of the effects of centrifugal force in rotating convection, although Koschmieder (1993) extensively discusses its importance in interpreting experimental observations. One very recent exception is Becker *et al.* (2006) who have shown through both experiments and numerical simulation that the centrifugal force has a significant influence on the quantitative features of domain chaos in large-aspect-ratio rotating convection with relatively slow rotation (they considered systems with $\gamma \in (20, 80)$, $\Omega \in [15, 19]$ and $\sigma = 0.88$). They concluded that rotating convection experiments with large aspect ratios will be severely influenced by centrifugal-force effects.

We find that for $\gamma = 1$, $\Omega = 100$ and $\sigma = 7$, the centrifugally driven axisymmetric LSC dominates the rotating convection problem as the Froude number increases. For faster rotation (larger Ω) in larger-aspect-ratio cylinders, with all else being equal,

the influence of centrifugal buoyancy can be expected to be even greater, providing an even stronger quenching of non-axisymmetric disturbances.

This work was supported by the Spanish grants FIS2004-01336 and BFM2003-00657, Catalan grant SGR-00024, and the National Science Foundation grant DMS-0509594.

REFERENCES

Barcilon, V. & Pedlosky, J. 1967 On the steady motions produced by a stable stratification in a rapidly rotating fluid. *J. Fluid Mech.* **29**, 673–690.

Barkley, D. & Tuckerman, L. S. 1988 Global bifurcation to traveling waves in axisymmetric convection. *Phys. Rev. Lett.* **61**, 408–411.

Becker, N., Scheel, J. D., Cross, M. C. & Ahlers, G. 2006 Effect of the centrifugal force on domain chaos in Rayleigh-Bénard convection. *Phys. Rev. E* **73**, 066309.

Bergeon, A., Henry, D., Benhadid, H. & Tuckerman, L. S. 1998 Marangoni convection in binary mixtures with Soret effect. *J. Fluid Mech.* **375**, 143–177.

Bodenschatz, E., Pesch, W. & Ahlers, G. 2000 Recent developments in Rayleigh-Bénard convection. *Annu. Rev. Fluid Mech.* **32**, 709–778.

Buell, J. C. & Catton, I. 1983 Effect of rotation on the stability of a bounded cylindrical layer of fluid heated from below. *Phys. Fluids* **26**, 892–896.

Chandrasekhar, S. 1961 *Hydrodynamic and Hydromagnetic Stability*. Oxford University Press.

Fornberg, B. 1998 *A Practical Guide to Pseudospectral Methods*. Cambridge University Press.

Frayssé, V., Giraud, L. & Langou, J. 2003 A set of GMRES routines for real and complex arithmetics on high performance computers. *Tech. Rep.* TR/PA/03/3. CERFACS.

Goldstein, H. F., Knobloch, E., Mercader, I. & Net, M. 1993 Convection in a rotating cylinder. Part 1. Linear theory for moderate Prandtl numbers. *J. Fluid Mech.* **248**, 583–604.

Goldstein, H. F., Knobloch, E., Mercader, I. & Net, M. 1994 Convection in a rotating cylinder. Part 2. Linear theory for low Prandtl numbers. *J. Fluid Mech.* **262**, 293–324.

Hart, J. E. 2000 On the influence of centrifugal buoyancy on rotating convection. *J. Fluid Mech.* **403**, 133–151.

Herrmann, J. & Busse, F. H. 1993 Asymptotic theory of wall-attached convection in a rotating fluid layer. *J. Fluid Mech.* **255**, 183–194.

Homsy, G. M. & Hudson, J. L. 1969 Centrifugally driven thermal convection in a rotating cylinder. *J. Fluid Mech.* **35**, 33–52.

Homsy, G. M. & Hudson, J. L. 1971 Centrifugal convection and its effect on the asymptotic stability of a bounded rotating fluid heated from below. *J. Fluid Mech.* **48**, 605–624.

Hughes, S. & Randriamampianina, A. 1998 An improved projection scheme applied to pseudospectral methods for the incompressible Navier-Stokes equations. *Intl. J. Numer. Meth. Fluids* **28**, 501–521.

Koschmieder, E. L. 1993 *Bénard Cells and Taylor Vortices*. Cambridge University Press.

Kuo, E. Y. & Cross, M. C. 1993 Traveling-wave wall states in rotating Rayleigh-Bénard convection. *Phys. Rev.* E **47**, R2245–R2248.

Kuznetsov, Y. A. 1998 *Elements of Applied Bifurcation Theory*, 2nd edn. Springer.

Lopez, J. M., Rubio, A. & Marques, F. 2006 Traveling circular waves in axisymmetric rotating convection. *J. Fluid Mech.* **569**, 331–348.

Mamun, L. S. & Tuckerman, L. S. 1995 Asymmetry and Hopf bifurcation in spherical Couette flow. *Phys. Fluids* **7**, 80–91.

Mercader, I., Batiste, O. & Alonso, A. 2006 Continuation of travelling-wave solutions of the Navier-Stokes equations. *Intl J. Numer. Meth. Fluids* **52**, 707–721.

Mercader, I., Net, M. & Falqués, A. 1991 Spectral methods for high order equations. *Comput. Meth. Appl. Mech. Engng* **91**, 1245–1251.

Ning, L. & Ecke, R. E. 1993 Rotating Rayleigh-Bénard convection: Aspect-ratio dependence of the initial bifurcations. *Phys. Rev.* E **47**, 3326–3333.

Orszag, S. A. & Patera, A. T. 1983 Secondary instability of wall-bounded shear flows. *J. Fluid Mech.* **128**, 347–385.

Pfotenhauer, J. M., Niemela, J. J. & Donnelly, R. J. 1987 Stability and heat transfer of rotating cryogens. Part 3. Effects of finite cylindrical geometry and rotation on the onset of convection. *J. Fluid Mech.* **175**, 85–96.

Rossby, H. T. 1969 A study of Benard convection with and without rotation. *J. Fluid Mech.* **36**, 309–335.

Sánchez-Álvarez, J. J., Serre, E., Crespo del Arco, E. & Busse, F. H. 2005 Square patterns in rotating Rayleigh-Bénard convection. *Phys. Rev.* E **72**, 036307.

Veronis, G. 1959 Cellular convection with finite amplitude in a rotating fluid. *J. Fluid Mech.* **5**, 401–435.

Zhong, F., Ecke, R. & Steinberg, V. 1991 Asymmetric modes and the transition to vortex structures in rotating Rayleigh-Bénard convection. *Phys. Rev. Lett*. **67**, 2473–2476.

Zhong, F., Ecke, R. & Steinberg, V. 1993 Rotating Rayleigh-Bénard convection: asymmetric modes and vortex states. *J. Fluid Mech.* **249**, 135–159.